

# CFD Modeling: Different Kinetic Approaches for Internal Reforming Reactions in an Anode-Supported SOFC

Hedvig Paradis<sup>1</sup>  
e-mail: hedvig.paradis@energy.lth.se

Martin Andersson

Jinliang Yuan

Bengt Sundén

Department of Energy Sciences,  
Faculty of Engineering,  
Lund University,  
P.O. Box 118,  
221 00 Lund, Sweden

Fuel cells are electrochemical devices that convert chemical energy into electricity. Solid oxide fuel cells (SOFCs) are a particularly interesting type because they can reform hydrocarbon fuels directly within the cell, which is possible, thanks to their high operating temperature. The purpose of this study is to develop an anode-supported SOFC theoretical model to enhance the understanding of the internal reforming reactions and their effects on the transport processes. A computational fluid dynamics approach, based on the finite element method, is implemented to unravel the interaction among internal reforming reactions, momentum, and heat and mass transport. The three different steam reforming reaction rates applied were developed and correlated with experimental studies found in the literature. An equilibrium rate equation is implemented for the water-gas shift reaction. The result showed that the reaction rates are very fast and differ quite a lot in size. The pre-exponential values, in relation to the partial pressures, and the activation energy affected the reaction rate. It was shown that the anode structure and catalytic composition have a major impact on the reforming reaction rate and cell performance. The large difference between the different activation energies and pre-exponential values found in the literature reveals that several parameters probably have a significant influence on the reaction rate. As the experiments with the same chemical compositions can be conducted on a cell or only on a reformer, it is important to reflect over the effect this has on the kinetic model. To fully understand the effect of the parameters connected to the internal reforming reaction, microscale modeling is needed. [DOI: 10.1115/1.4002906]

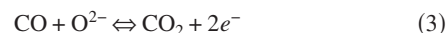
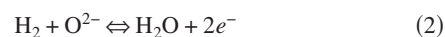
**Keywords:** SOFC, modeling, internal reforming reactions, anode-supported, transport processes

## 1 Introduction

Fuel cells are energy conversion devices that produce electricity and heat directly from a hydrogen-based fuel through electrochemical reactions when the device is fed with an oxidant. SOFC is a high temperature cell that operates at 600–1000°C [1]. If the electrolyte is kept thin, it is possible to reduce the temperature to a moderate level (600–800°C [1]) and still maintain the environment for the internal reforming reaction. A single SOFC consists of an air channel and a fuel channel, two porous electrodes that are separated by an electrolyte. The fuel electrode is the anode and the oxidant electrode is the cathode. The electrolyte works as a passage for the ions and blockage for the electrons. The oxygen ions react with hydrogen and carbon monoxide in the fuel mixture at the anode/electrolyte interface and produce water and carbon dioxide while releasing electrons that flow via external circuits to the cathode/electrolyte. Unlike the porous electrode, the electrolyte should not be permeable for gas. The anode is usually nickel/zirconia cermet, which provides high electrochemical performance and good chemical stability, and the cathode is usually a perovskite material.

The aim of this study is to find out of how the internal reforming reactions of methane affect the physical processes. Because SOFCs operate at high temperature, they supply a sufficiently good condition to internally reform the hydrocarbon-based fuel

within the cells. For this reason, it is possible to work with a broader variety of fuels, e.g., methane, propane, or ethanol, besides hydrogen [2]. The following global reactions are considered in this model,



Equation (1) is the reduction of oxygen in the cathode. Equations (2) and (3) are the electrochemical reactions at the anodic three-phase boundary (TPB). TPB is the region where the electrolyte and electrode meet. Equation (4) is the steam reforming of methane (usually called catalytic steam reforming reaction), which needs to be carried out before the electrochemical reactions. Carbon monoxide can be oxidized as in Eq. (3) or react with water as in Eq. (5). Equation (5) is often called the water-gas shift reforming reaction.

## 2 Mathematical Model

A computational fluid dynamics (CFD) approach is applied to solve the equations for momentum and heat and mass transport simultaneously. A two-dimensional model is adopted for the anode-supported SOFC and implemented in COMSOL MULTIPHYS-

<sup>1</sup>Corresponding author.

Contributed by the Advanced Energy Systems Division of ASME for publication in the JOURNAL OF FUEL CELL SCIENCE AND TECHNOLOGY. Manuscript received August 17, 2010; final manuscript received September 21, 2010; published online March 1, 2011. Editor: Nigel M. Sammes.

**Table 1 Cell dimensions [1]**

Part of the cell	Size (mm)
Cell length	100
Air channel height	1
Fuel channel height	1
Electrolyte height	0.02
Cathode height	0.05
Anode height	0.5
Interconnect height	0.5

ICS. The geometry is defined in Table 1 and a sketch of the model is shown in Fig. 1.

**2.1 Mass Transport.** To represent the mass transport for the gases within the cell, the Maxwell–Stefan equation for mass diffusion and convection is used. The Maxwell–Stefan equation is a simplified equation of the Dusty gas model. For flows with low velocity in the porous medium, it is often assumed that the transport process is dominated by diffusion [3]. The Knudsen term is used when the pores are small compared with the free mean path of the gas [1,4]. The Knudsen diffusion is neglected in study to save computational cost. The Maxwell–Stefan equation is defined for the domain including the electrodes and the fuel and air channels, as follows [1]:

$$\nabla \left( -\rho \cdot w_i \sum D_{ij} \cdot \nabla x_j + (x_j - w_j) \cdot \frac{\nabla p}{p} \cdot u - D_i^T \cdot \frac{\nabla T}{T} \right) + \rho \cdot u \cdot \nabla w_j = S_i \quad (6)$$

where  $w$  is the mass fraction,  $D_{ij}$  is the Maxwell–Stefan binary diffusion coefficient,  $x$  is the mole fraction,  $D_i^T$  is the thermal diffusion coefficient, and  $S_i$  is the source term.  $S_i$  is zero for the electrochemical reactions because they are assumed, in this study, to take place at the interfaces between the electrolyte and electrodes. This is possible because the active layer is considered to be very thin compared with the thick electrode [5]. They are therefore defined as an interface condition instead. The diffusion coefficient in the porous electrodes is  $D_{ij,por}$ , calculated as [1]

$$D_{ij,por} = D_{ij} \cdot \frac{\varepsilon_p}{t} \quad (7)$$

where  $\varepsilon_p$  is the porosity and  $t$  is the tortuosity.

The mass or molar fractions for the air and fuel channel inlets are defined and the outlet conditions are defined as the convective flux.

**2.2 Heat Transport.** The heat transfer within the cell consists of convection between the solid surface and the gas flow, conduc-

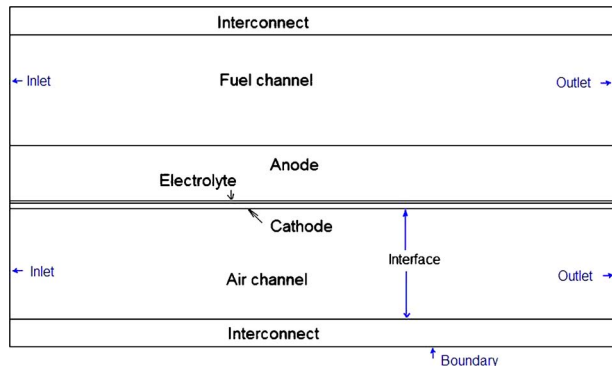


**Fig. 1 Schematic figure of a unit cell in an anode-supported SOFC model, not to scale**

tion in the solid and the porous parts, and heat generation/consumption occurs due to the electrochemical reactions at the TPB as well as the internal reforming reactions. Thermal radiation is not included in this study as the cell is considered to be in the middle of the stack surrounded by cells with the same boundary condition for the temperature (symmetry). If thermal radiation between the walls and gas mixtures is considered, it could have some influence on the results. The prediction of the temperature distribution can either be conducted by a local thermal equilibrium (LTE) or a local thermal nonequilibrium (LTNE) approach. For this study, the LTNE approach is used due to low Reynolds number and large differences in thermal conductivities between the gas and solid phases. The temperature distribution is calculated separately for the gas and solid phases. The general heat conduction equation is used to calculate the temperature distribution for the solid medium in the porous electrodes [1],

$$\nabla(-k_s \cdot \nabla T_s) = Q_s \quad (8)$$

where  $k_s$  is thermal conductivity for the solid media,  $T_s$  is the temperature in the solid phase, and  $Q_s$  is the heat source (heat transfer between the gas and solid phases, the heat generation due to the Ohmic polarization and due to the internal reforming reactions). The temperature for the gas phase in the fuel gas and air channels and the porous electrodes are calculated as

$$\nabla(-k_g \cdot \nabla T_g) = Q_g - \rho_g \cdot c_{p,g} \cdot u \cdot \nabla T_g \quad (9)$$

where  $T_g$  is the gas temperature,  $c_{p,g}$  is the heat capacity,  $k_g$  is the gas conductivity, and  $Q_g$  is the heat transfer between the gas and solid phases. Because the Reynolds number is low, the heat transfer coefficient  $h_{s,g,por}$  (when spherical particles are assumed in the porous electrodes) can be calculated as [1]

$$h_{s,g,por} = \frac{2 \cdot k_g}{d_p} \quad (10)$$

where  $d_p$  is the electrode particle diameter. The heat transfer between the gas and solid phases is defined as

$$Q_g = -Q_s = h_v \cdot (T_g - T_s) = AV \cdot h_{s,g,por} \cdot (T_g - T_s) \quad (11)$$

where  $h_v$  is the volume heat transfer coefficient and  $AV$  the active surface area to volume ratio.

The boundaries at the top and the bottom of the cell model are defined by symmetries since the cell is considered to be surrounded by other similar cells with the same temperature distribution. The temperatures at the air and fuel channel inlets are defined as constant and at the outlets the boundaries are defined as the convective flux.

**2.3 Momentum Transport.** The approach to momentum equation is selected to separately solve the Darcy's equation for the porous electrodes and the Navier–Stokes equations for the channels. The Darcy–Brinkman equation is then used to solve the gas flow in the gas phase [1],

$$\left( \frac{\mu}{\kappa} + \rho \cdot \nabla u \right) \cdot u - \nabla \left[ -p + \frac{1}{\varepsilon_p} \cdot \{T - (\lambda - \kappa_{dv}) \cdot (\nabla u)\} \right] = F \quad (12)$$

where  $\mu$  is the dynamic viscosity,  $\kappa$  is the permeability of the porous medium,  $\varepsilon_p$  is the porosity,  $T$  is the viscous stress tensor, and  $F$  is the volume force vector.  $\lambda$  is the second viscosity and for gases it is normally set to  $\lambda = -2/3 \cdot \mu$  [1].  $\kappa_{dv}$  is the deviation from the thermodynamic equilibrium and is by default set to zero. The Darcy–Brinkman equation is converted into the Darcy equation when the Darcy number  $Da \rightarrow 0$  in the porous layers and into the Navier–Stokes equation when  $\kappa \rightarrow \infty$  and  $\varepsilon_p = 1$  in the fuel and air channels.

The velocity profile is defined at the air and fuel channel inlets as the laminar flow and the pressure at the outlets.

**2.4 Electrochemical Reactions.** The electrochemical reactions occur at the TPB. Ions migrate in the ionic phase and conduction of the electrons occurs in the electronic phase. The electrolyte functions on one hand to transport the oxygen ions to the anode and, on the other hand, to block the electrons crossing from the anode to the cathode. The flow of electronic charges through the external circuit balances the flow of ionic charges through the electrolyte. This transport is described in terms of the ion transport from the conservation of charge [1],

$$\nabla \cdot i = 0 = \nabla \cdot i_{io} + \nabla \cdot i_{el} \quad (13)$$

$$-i_{io} = \nabla \cdot i_{el} \quad (14)$$

$$i_{io} = -\sigma_{io}^{eff} \cdot \nabla \phi_{io} \quad (15)$$

where  $i_{io}$  and  $i_{el}$  are charge fluxes for ions and electrons, respectively, and  $\phi_{io}$  is the ionic potential in the electrolyte. The Nernst potential is calculated as the sum of the potential differences across the anode and the cathode as [1]

$$E = \Delta \phi_a + \Delta \phi_c \quad (16)$$

where  $E$  is the reversible electrochemical cell voltage and  $\phi$  is the charge potential. At the interface between the electrode and electrolyte, the Butler–Volmer equation is used to calculate the volumetric current density [1],

$$i = i_0 \left\{ \exp \left( \beta \cdot \frac{n_e \cdot F \cdot \eta_{act,e}}{R \cdot T} \right) - \exp \left( -(1 - \beta) \cdot \frac{n_e \cdot F \cdot \eta_{act,e}}{R \cdot T} \right) \right\} \quad (17)$$

where  $i_0$  is the exchange current density,  $F$  is the Faraday constant,  $\beta$  is the transfer coefficient,  $n_e$  is the number of electrons transferred per reaction,  $\eta_{act,e}$  is the electrode activation polarization overpotential, and finally  $R$  is the ideal gas constant. If the transfer coefficient  $\beta$  is assumed to be 0.5, the Butler–Volmer equation is reduced to

$$i = 2 \cdot i_0 \cdot \sinh \left( \frac{n_e \cdot F \cdot \eta_{act,e}}{2 \cdot R \cdot T} \right) \quad (18)$$

$$\eta_{act,e} = \frac{2 \cdot R \cdot T}{n_e \cdot F} \sinh^{-1} \left( \frac{i}{2 \cdot i_{0,e}} \right) \quad (19)$$

$$i_0 = \frac{R \cdot T}{n_e \cdot F} \cdot k'' \cdot \exp \left( \frac{-E_e}{R \cdot T} \right) \quad (20)$$

where  $k''$  is the pre-exponential factor and  $E$  is the activation energy. The gas species distributions are implemented by source terms due to the electrochemical reaction as [1,6]

$$r_{H_2} = \frac{-i}{2 \cdot F} \quad (21)$$

$$r_{H_2O} = \frac{i}{2 \cdot F} \quad (22)$$

$$r_{O_2} = \frac{-i}{4 \cdot F} \quad (23)$$

where  $i$  is the current density and  $F$  is the Faraday constant.

**2.5 Internal Reforming Reactions.** The internal reforming reaction rates are taken into account by the source terms in the Maxwell–Stefan equation. The mass source terms due to the reforming reactions are expressed as

$$S_{H_2} = (3r_r + r_s) \cdot M_{H_2} \quad (24)$$

$$S_{CH_4} = -r_r \cdot M_{CH_4} \quad (25)$$

$$S_{H_2O} = (-r_r - r_s) \cdot M_{H_2O} \quad (26)$$

$$S_{CO} = (r_r - r_s) \cdot M_{CO} \quad (27)$$

The equation for  $CO_2$  can be solved separately because the sum of the mass fractions is equal to unity. The reaction rate  $r_r$  is for the catalytic steam reforming reaction and  $r_s$  is for the water-gas shift reaction.

The reaction rates for the methane steam reforming reaction are evaluated by kinetic models and for the water-gas shift reaction an equilibrium approach is applied. The three reaction kinetic approaches applied are from Refs. [7–11]. It is worth noting that both Achenbach and Riensche's [8,9] kinetics (Eq. (28)) together with Leinfelder's [10] (Eq. (29)) kinetics are an Arrhenius kinetics reaction rate type, while Drescher's kinetics [11] (Eq. (30)) is a Langmuir–Hinshelwood type. They are selected on the basis of the different order of the partial pressure and the broad range of the activation energy. The kinetics differences depend on how the experimental configuration is set up, and the material decomposition and operating conditions are selected. Equation (28) is found by the combination of both the study of Achenbach and Riensche [8] and the study of Achenbach [9], where it could be found that the reaction order of the partial pressure of methane is unity and the partial pressure of water has no catalytic effect on the reaction, which leads to the simplified equation [8,9]. Note that Leinfelder [10] found a positive reaction order of water and Achenbach and Riensche [8,9] found a reaction order of zero.

The reaction rates from these three different experimental studies are shown below,

$$r_{r,AchRie} = 4274 \cdot p_{CH_4} \cdot \exp \left( \frac{-82,000}{R \cdot T_s} \right) \cdot AV \quad (28)$$

$$r_{r,Lei} = 30.8 \times 10^{10} \cdot p_{CH_4} \cdot p_{H_2O} \cdot \exp \left( \frac{-205,000}{R \cdot T_s} \right) \cdot AV \quad (29)$$

$$r_{r,Dre} = \frac{288.52 \cdot p_{CH_4} \cdot p_{H_2O} \cdot \exp \left( \frac{-11,000}{R \cdot T_s} \right)}{1 + 16.0 \cdot p_{CH_4} + 0.143 \cdot p_{H_2O} \cdot \exp \left( \frac{39,000}{R \cdot T_s} \right)} \cdot AV \quad (30)$$

where  $p$  is the partial pressure and  $T_s$  is the solid phase temperature.  $AV$  is the active surface area to volume ratio. The units for all the steam reforming reaction rates are  $\text{mol/s m}^3$ .

The reaction rates above are described from the global kinetic point of view, which only depends on a few parameters. As it appears not to be sufficient to only describe the reaction rates with a few empirical parameters, it is necessary to develop a suitable micromodel for the SOFC. However, the global kinetic models may still predict valuable behaviors.

The reaction rate equations (Eqs. (28) and (29)) are of the Arrhenius type. The rate equation consists of three parts, partial pressures, pre-exponential factor, and activation energy. These parameters differ quite a lot in the literature among different research works. The pre-exponential factor describes the number of collisions between the molecules within the reaction. The exponential expression with activation energy describes the probability for the reaction to occur. As the activation energy increases, the catalytic reaction becomes less probable. The activation energy is based on the catalytic characteristics, such as chemical composition. Even though the activation energy may be high, which lead to a decrease in the reaction rate, the overall reaction rate however can still be fast due to the pre-exponential value. The pre-exponential factors depend strongly on both the temperature and properties of the anode material. It is possible to change the reaction rate, either by changing the particle size of the active catalysts or the porous structure, i.e., the active catalytic area. The large

difference between the activation energies found in the literature [1,7–12] suggests that more parameters have significant influence on the reaction rate.

According to Nagel et al. [7], a small steam-to-carbon (SC) ratio yields positive reaction orders and a high SC ratio yields negative reaction orders. For this study, the steam to carbon ratio is around 2, which agrees with the three kinetic models. Achenbach and Riensche [8,9] applied a 14 mm thick nickel cermet semidisk consisting of 20 wt % Ni and 80 wt % ZrO<sub>2</sub> (stabilized). The active surface area was  $3.86 \times 10^{-4}$  m<sup>2</sup>. The temperature was varied from 700 °C to 940 °C and the system pressure from 1.1 bar to 2.8 bar. Leinfelder [10] applied a 50 μm thick anode built up by two layers with 64 wt % Ni and 36 wt % YSZ and 89 wt % Ni and 11 wt % YSZ, respectively. The active surface area for the anode was  $2.5 \times 10^{-3}$  m<sup>2</sup>. The test was conducted for temperatures of 840–920 °C and at a pressure of 1 bar. Drescher [11] applied an anode consisting of 50 wt % Ni and 8 mol % YSZ. Achenbach and Riensche's model is based on a work on a reformer, while the other two, Leinfelder's and Drescher's, are based on a unit cell.

In this study, the temperature is varied from 727 °C to 827 °C (1000–1100 K) since this is the range within which the experiments were carried out. The active surface area to volume ratio is varied between  $10 \times 10^4$  m<sup>2</sup>/m<sup>3</sup> and  $5 \times 10^5$  m<sup>2</sup>/m<sup>3</sup>. The active surface area to volume ratio has been adopted according to a common used value in the literature [6,12–16]. Several authors have applied an active surface area to volume ratio of  $5 \times 10^5$  for modeling work. Janardhanan and Deutschmann [6] applied a slightly smaller surface area to volume ratio of 102,500 m<sup>2</sup>/m<sup>3</sup>, whereas Klein et al. [12] applied a much larger value of  $2.2 \times 10^6$  m<sup>2</sup>/m<sup>3</sup>. Note that only a small part of the whole active surface acts as a locus for the chemical reactions. The trend for the development during the past years is in the direction of employing smaller particles to get a larger AV.

The water-gas shift reaction is considered to be very quick and to remain in equilibrium by several authors in the literature [5,12,17]. The equilibrium approach in the fuel channel and the anode can be defined as

$$r_s = k_s \cdot p_{\text{CO}} \cdot \left( 1 - \frac{p_{\text{CO}_2} \cdot p_{\text{H}_2}}{K_{e,s} \cdot p_{\text{CO}} \cdot p_{\text{H}_2\text{O}}} \right) \quad (31)$$

$$K_{e,s} = \exp\left(\frac{4276}{T} - 3.961\right) \quad (32)$$

where  $k_s$  is the reaction rate constant and  $K_{e,s}$  is the equilibrium constant for the water-gas shift reaction. The value for  $k_s$  is calculated according to Haberman and Young [18]. The unit for the water-gas shift reaction rate is mol/s m<sup>3</sup>. The heat generation and heat consumption are defined as source terms in the governing equations. The heat generation in the fuel channel enters in the gas phase. The heat generation and the heat consumption are assumed to occur on the solid surface. The heat generation and heat consumption due to the reforming reactions are implemented in Eq. (8) and defined as

$$Q_{\text{int,ref}} = \sum_i r_i \cdot \Delta h_{\text{reac},i} \quad (33)$$

where  $\Delta h_{\text{reac}}$  is the enthalpy change due to the reactions and  $Q_{\text{int,ref}}$  is the heat generation.

### 3 Results and Discussion

**3.1 Base Conditions.** According to the standards by the International Energy Agency (IEA) [1], the inlet temperature was specified to be 1000 K (727 °C) both for the air and fuel channels. The fuel composition for 30% pre-reformed natural gas is defined by IEA and is frequently used in the literature. The catalytic active surface area to volume ratio  $10 \times 10^5$  m<sup>2</sup>/m<sup>3</sup> is a reappearing

**Table 2 Inlet mole fraction for the fuel gas species [1]**

Fuel gas species	Inlet mole fraction
H <sub>2</sub>	0.2626
CH <sub>4</sub>	0.171
CO	0.0294
H <sub>2</sub> O	0.4934
CO <sub>2</sub>	0.0436

value found in the literature. The average cell current density is specified to be 0.3 A/cm<sup>2</sup>. The 30% pre-reformed natural gas is supplied by external reformers, and the inlet conditions are specified in Table 2. The material characteristics are specified in Table 3. The model has been checked for all cases to fulfill the requirement of grid independency.

The flow direction is set to be from left to right for air and fuel channels as well as the anode and the cathode. It should be explicitly mentioned that the length of the cell is 100 times longer than the height of the air or the fuel channel.

The predicted gas phase temperature in the cell is plotted in Figs. 2–4 for Achenbach and Riensche's, Leinfelder's, and Drescher's kinetics, respectively. There is a decrease in temperature after a short distance from the inlet for both the fuel and air channels. In the fuel channels, it is due to the steam reforming reaction, which consumes the heat when the methane is reformed to hydrogen and carbon monoxide. The temperature on the air side is lower due to a higher air flow rate. The decrease in temperature close to the inlet is 50 K for both Achenbach and Riensche's and Leinfelder's kinetics. The area of the temperature drop is larger for Achenbach and Riensche's kinetics than those from both Leinfelder's and Drescher's kinetics. But the recovery to a higher temperature occurs faster for both Leinfelder's and Drescher's kinetics than for Achenbach and Riensche's kinetics, the latter of which is affected by the fast conversion of methane to hydrogen and carbon monoxide. The temperature distribution for Drescher's ki-

**Table 3 Material characteristics data [1,4,6]**

Anode thermal conductivity, $k_{s,a}$	11 W/m K
Cathode thermal conductivity, $k_{s,c}$	6 W/m K
Electrolyte thermal conductivity, $k_{s,el}$	2.7 W/m K
Interconnect thermal conductivity, $k_{s,int}$	20 W/m K
Anode heat capacity, $c_{p,a}$	450 J/kg K
Cathode heat capacity, $c_{p,c}$	430 J/kg K
Electrolyte heat capacity, $c_{p,el}$	470 J/kg K
Interconnect heat capacity, $c_{p,int}$	550 J/kg K

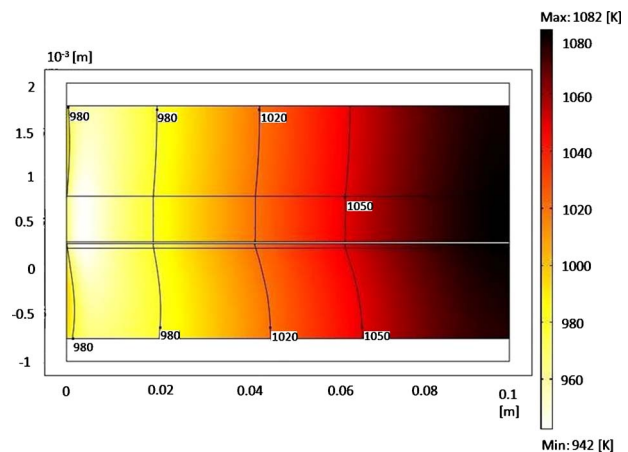


**Fig. 2 Temperature distribution (K) for Achenbach and Riensche's kinetics**

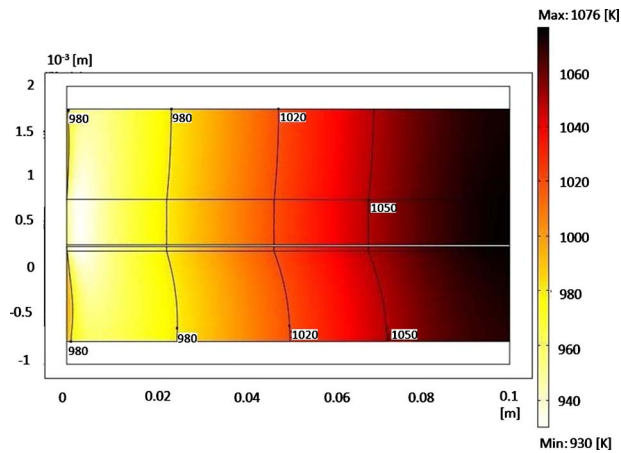


Fig. 3 Temperature distribution (K) for Leinfelder's kinetics

netics does not drop initially as much as the other two. A higher maximum temperature is also obtained for Drescher's kinetics. Note that the labels of the temperature range are different for each case. But the plotted temperature lines in the figures are the same for every condition and kinetics, i.e., 980 K, 1020 K, and 1050 K. The maximum and minimum temperatures are printed for each case as well.

The effect on mole fraction distribution for the different gas species is similar for both Achenbach and Riensche's and Leinfelder's kinetics and, therefore, only the mole fraction distribution for Leinfelder's kinetics is presented in Fig. 5. Methane reacts with steam at the surface of the Ni-catalyst in the anode, which leads to the production of carbon monoxide and hydrogen. The hydrogen is consumed at the TPB for the electrochemical reactions. As shown in Fig. 6, Drescher's kinetics obtained the maximum mole fraction of hydrogen faster and a higher maximum mole fraction than Achenbach and Riensche's and Leinfelder's kinetics. The initial consumption of water and the initial generation of hydrogen for Drescher's kinetics result in larger gradients of the mole fractions. All three kinetics are fast although Drescher's kinetics, expressed by a Langmuir-Hinshelwood type, differs slightly more from the others. It deserves to be pointed out that Drescher's kinetics includes both positive and negative orders of the partial pressure of methane and water, as well as two different activation energies for the denominator and the numerator, which can have some effect on the results.

The reaction rates for both the steam reforming reaction and the water-gas shift reaction are plotted in Figs. 7-9 for Achenbach and Riensche's, Leinfelder's, and Drescher's kinetics, respectively. It

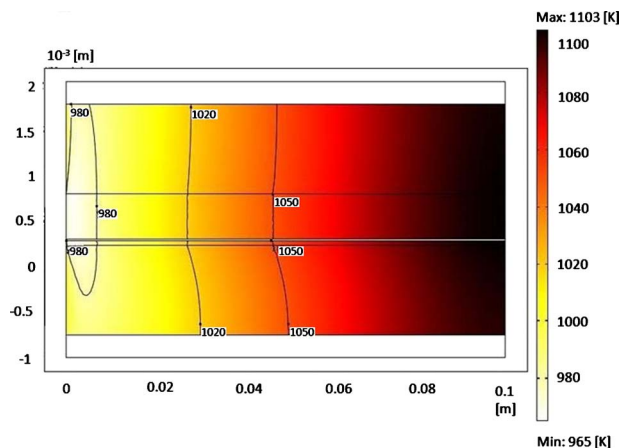


Fig. 4 Temperature distribution (K) for Drescher's kinetics

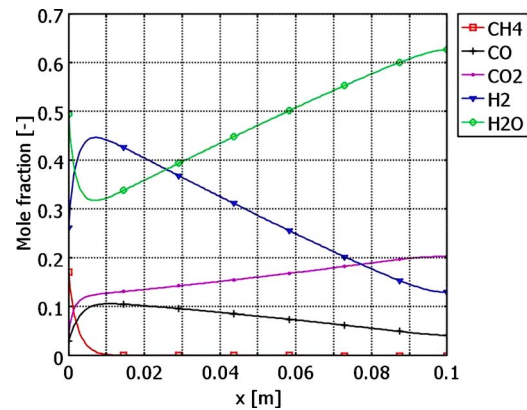


Fig. 5 Mole fraction of the gas species in the fuel channel along the flow direction for Leinfelder's kinetics

should be clearly noted that the reaction rates are only plotted for the entrance region, through 0.01 m. For Achenbach and Riensche's kinetics, the distribution of the steam reforming reaction rate is plotted in detail in Fig. 10. Close to the inlet where the concentration of methane is high, the reaction rate for the steam reforming reaction is high. All of the anode depth is used for the reaction. As shown in the figures, the reaction rate for the steam reforming and the water-gas shift is much faster for Drescher's kinetics than for both Achenbach and Riensche's and Leinfelder's kinetics. Yet, Leinfelder's kinetics is faster than Achenbach and

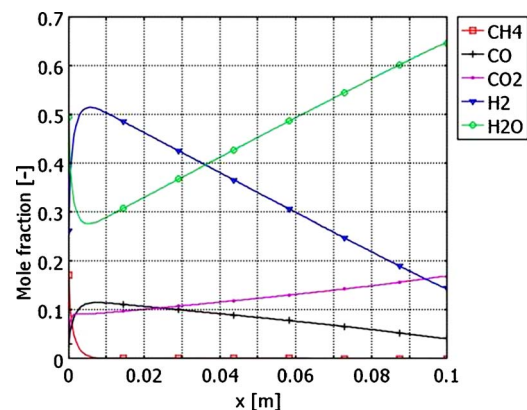


Fig. 6 Mole fraction of the gas species in the fuel channel along the flow direction for Drescher's kinetics

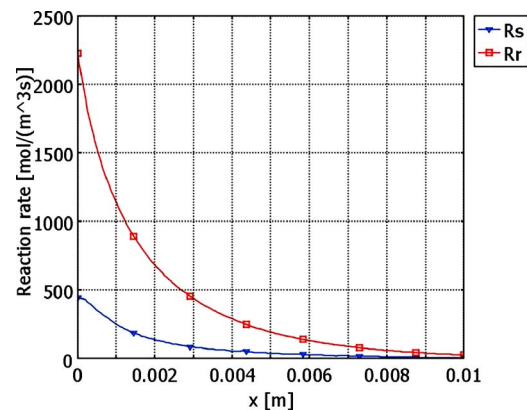


Fig. 7 Reforming reaction rate ( $\text{mol}/\text{m}^3 \text{ s}$ ) for the entrance region (until 0.01 m) along the flow direction for Achenbach and Riensche's kinetics

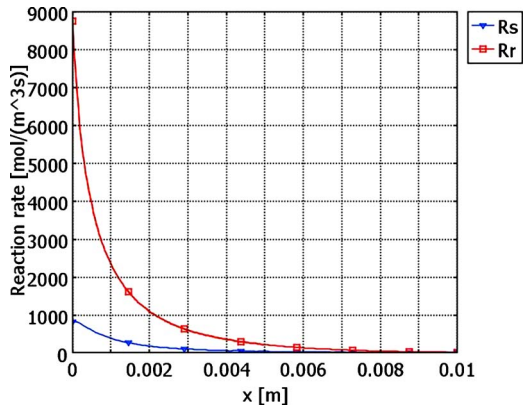


Fig. 8 Reforming reaction rate ( $\text{mol}/\text{m}^3 \text{ s}$ ) for the entrance region (until 0.01 m) along the flow direction for Leinfelder's kinetics

Riensché's. Close to the inlet in the anode where carbon monoxide generation is high, the reaction rate for the water-gas shift reaction is at the highest. The high generation of carbon monoxide is due to the steam reforming reaction. Furthermore, more hydrogen is produced when steam is generated due to the fact that the water-gas shift equation is in equilibrium through the process. As

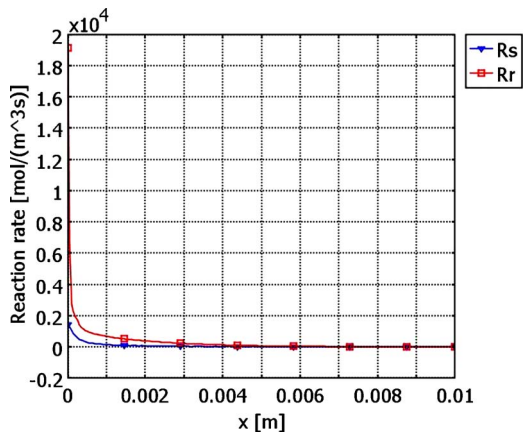


Fig. 9 Reforming reaction rate ( $\text{mol}/\text{m}^3 \text{ s}$ ) for the entrance region (until 0.01 m) along the flow direction for Drescher's kinetics

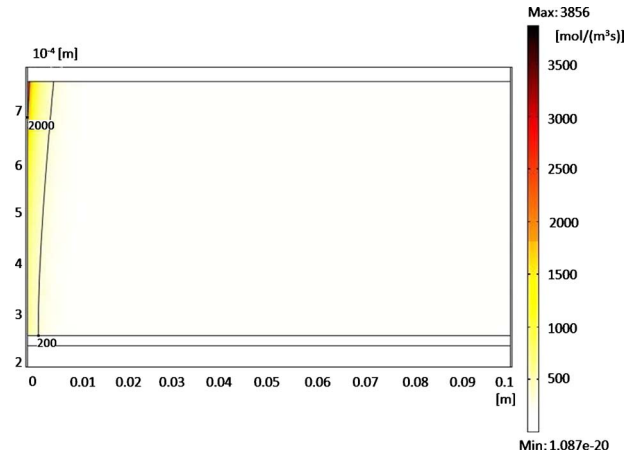


Fig. 10 Distribution of the steam reforming reaction rate in the anode for Achenbach and Riensché's kinetics

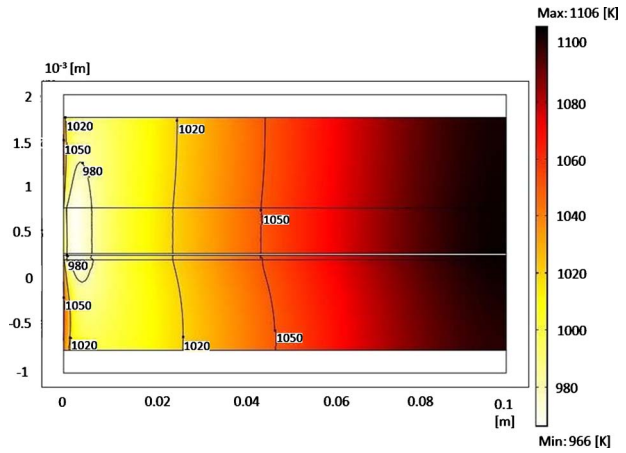


Fig. 11 Temperature distribution (K) for Leinfelder's kinetics ( $T=1100 \text{ K}$ )

hydrogen is consumed, steam is generated thanks to the electrochemical reaction at the TPB. The reaction rate for the water-gas shift reaction reaches a higher value due to the faster reaction rate for the steam reforming reaction for Drescher's and Leinfelder's kinetics compared with Achenbach and Riensché's kinetics. The comparison between the different kinetic models need to be evaluated on a more detailed level as it cannot be correctly explained by just a few empirical parameters, such as the activation energy and the pre-exponential value. To fully understand the effect and dependency of the parameters, micromodeling is needed. What can be concluded from this study is that the configuration and geometrical properties of the anode and the chemical composition and catalytic characteristics are important. To draw confirmatory conclusions from the modeling work, it is important to reveal the difference of the kinetic models from the experimental work carried out on SOFC and a reformer based on the same properties.

**3.2 Temperature Effects.** A parameter study was carried out for Leinfelder's kinetics because it is found, based on the above discussion, that the reaction rates for Leinfelder's kinetics are not as fast as Drescher's, but they are slightly faster than Achenbach and Riensché's. The inlet temperature was increased 50 K for Leinfelder's kinetics. The other parameters were kept the same as in the base case. The temperature distribution for both cases results in a similar way but obviously resulted in a higher temperature range, as shown in Fig. 11. The mole fraction distribution for the fuel gas species has the same range and trend as the base case. The reaction rates are slightly faster for a higher inlet temperature, but this is not shown here because of the similarity to the base case. In Fig. 12, the reaction rates are presented for Leinfelder's kinetics with an increased inlet temperature. Again, the reaction rates are only plotted for the entrance region, through 0.01 m. Due to the increased inlet temperature, the maximum reaction rates are almost doubled compared with the base case at the inlet.

**3.3 Active Surface Area to Volume Ratio Effects.** A parameter study was also conducted for the active surface area to volume ratio from  $10 \times 10^4 \text{ m}^2/\text{m}^3$  to  $5 \times 10^5 \text{ m}^2/\text{m}^3$ , which is a frequently used interval in the literature. All the other parameters were kept the same as the base case. The temperature profile is distributed in a similar overall trend as for the base case by comparing Figs. 3 and 13. The temperature was distributed in the same range for the two larger active surface area to volume ratios but the initial drop for the larger is greater than for a smaller one; however, compared with the base case, the minimum temperature differs by 20 K. Each mole fraction profile is distributed in a similar way as the specific base case for that mole fraction. The mole fractions reach approximately the same maximum value for the different active surface area to volume ratios but occur at

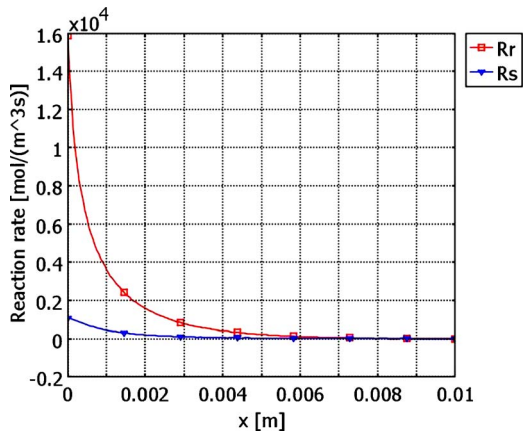


Fig. 12 Reforming reaction rate (mol/m<sup>3</sup> s) for the entrance region (until 0.01 m) along the flow direction for Leinfelder's kinetics (T=1100 K)

different distances from the inlet. A higher ratio results in the maximum of all the mole fraction species to occur closer to the inlet. In Fig. 14, the reaction rates for Leinfelder's kinetics with an increased active surface area to volume are presented. Again, the reaction rates are only plotted for the entrance region through 0.01

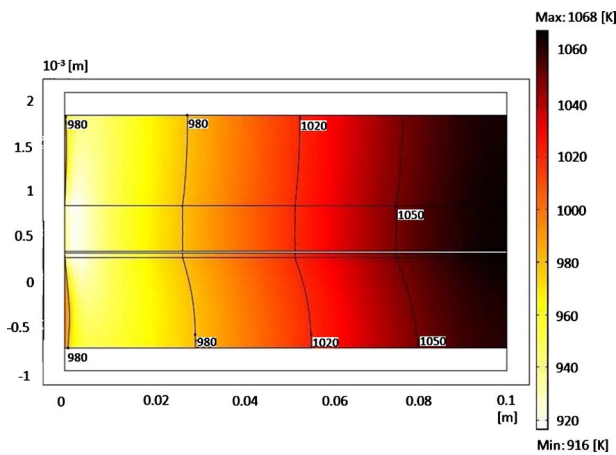


Fig. 13 Temperature distribution (K) for Leinfelder's kinetics (AV=5 E5)

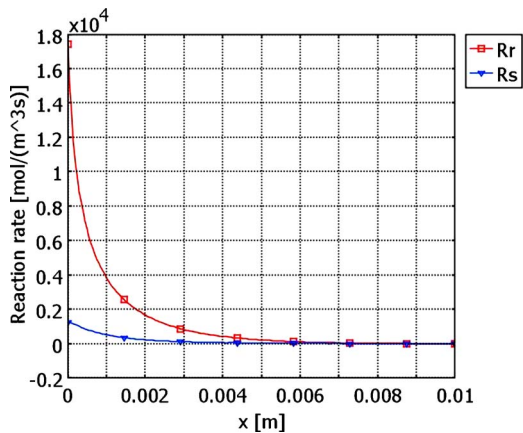


Fig. 14 Reforming reaction rate (mol/m<sup>3</sup> s) for the entrance region (until 0.01 m) along the flow direction for Leinfelder's kinetics (AV=5 E5)

m. The characteristics are distributed in a similar way for the reaction rates as for the base case, but the maximum value is more or less doubled for an increased active surface area to volume ratio. The reaction rates show the same trend when the inlet temperature is increased and similarly when the active surface area to volume ratio is increased. Similar maximum rates are obtained as the base case when an increased inlet temperature or an increased active surface area to volume ratio is used.

#### 4 Conclusions

In this study, a finite-element-based model for an anode-supported SOFC has been developed to better understand the internal reforming reactions of methane and the effects on the transport processes. The model has implemented COMSOL MULTIPHYSICS for the analysis of three different kinetic models. The equations for momentum and heat and mass transport are solved simultaneously. The three different reaction rates by experimental work found in the literature were examined. An equilibrium equation was employed for the water-gas shift reforming reaction rate. Parameter studies were also conducted for the inlet temperature and the active surface area to volume ratio.

The steam reforming reaction rates in this study are shown to be very fast. They differ slightly across the three models, which seems to be an effect of great differences of the pre-exponential value and the activation energy. Both these two parameters, pre-exponential value and activation energy, are connected to the partial pressure of methane and water. The model seems to be sensitive to the variation in the steam reforming reaction rate. Both the inlet temperature and the active surface area to volume ratio showed an effect on the reaction rates in terms of the maximum value. The temperature distributions were in the same range when the active surface area to volume ratio was increased. But with increased active surface area to volume ratio, the initial drop became much larger as the steam reforming reaction rate was subsequently increased. The reason why the different kinetics differs so much is that they are sensitive to how the experiment is designed.

The large difference between the different activation energies and pre-exponential values found in the literature shows that a larger number of parameters will have significant influence on the reaction rate, and to understand this relationship between the parameters, microscale modeling should be developed.

#### Acknowledgment

The financial support from the European Research Council (ERC) and the Swedish Research Council (VR) is gratefully acknowledged.

#### Nomenclature

- AV = active surface area to volume ratio, m<sup>2</sup>/m<sup>3</sup>
- $c_p$  = specific heat capacity at constant pressure, J/kg K
- $D_{ij}$  = Maxwell–Stefan binary diffusion coefficient, m<sup>2</sup>/s
- $D_l^T$  = thermal diffusion coefficient, kg/m s
- $\mathbf{F}$  = volume force vector, N/m<sup>3</sup>
- $h$  = enthalpy, J/mol
- $h_{s,g}$  = heat transfer coefficient, W/m<sup>2</sup> K
- $h_v$  = volume heat transfer coefficient, W/m<sup>3</sup> K
- $i$  = current density, A/cm<sup>2</sup>
- $i_0$  = exchange current density, A/cm<sup>2</sup>
- $k$  = thermal conductivity, W/m K
- $k'$  = Boltzmann's constant, J/K
- $k''$  = pre-exponential factor, 1/Ω m<sup>2</sup>
- $M_j$  = molar weight of species j, kg/mol
- $n_0$  = inlet mass flux, kg/m<sup>2</sup> s
- $n_e$  = number of electrons transferred per reaction
- $p$  = pressure, Pa

$Q$  = source term (heat),  $W/m^3$   
 $R$  = gas constant,  $8.314 \text{ J/mol K}$   
 $r$  = reaction rate,  $\text{mol}/m^2 \text{ s}$ ,  $\text{mol}/m^3 \text{ s}$   
 $S_i$  = source term (mass),  $\text{kg}/m^3 \text{ s}$   
 $\mathbf{T}$  = viscous stress tensor,  $N/m$   
 $T$  = temperature,  $K$   
 $u$  = velocity field,  $m/s$   
 $\nu$  = dynamic viscosity,  $Pa \cdot s$   
 $w_i$  = mass fraction of species  $i$ ,  $kg/kg$   
 $x_j$  = molar fraction of species  $j$ ,  $\text{mol}/\text{mol}$

### Greek Symbols

$\varepsilon_p$  = porosity, dimensionless  
 $\eta$  = overpotential,  $V$   
 $\kappa$  = permeability,  $m^2$   
 $\lambda$  = second viscosity,  $Pa \cdot s$   
 $\mu$  = dynamic viscosity,  $Pa \cdot s$   
 $\rho$  = density,  $kg/m^3$   
 $\sigma$  = ionic/electronic conductivity,  $\Omega^{-1} m^{-1}$

### Subscripts

$0$  = initial  
act = activation polarization  
 $e$  = electrode,  $e \in \{a, c\}$   
el = electrolyte  
 $g$  = gas phase  
 $i$  = molecule  $i$   
 $j$  = molecule  $j$   
 $p$  = porous media  
por = porous media  
 $r$  = steam reforming reaction  
 $s$  = solid phase, water-gas shift reaction

### Chemical

$CH_4$  = methane  
 $CO$  = carbon monoxide  
 $CO_2$  = carbon dioxide  
 $H_2$  = hydrogen  
 $H_2O$  = water  
 $O_2$  = oxygen  
 $Ni$  = nickel  
YSZ = yttria-stabilized zirconia

### References

- [1] Andersson, M., Yuan, J., and Sundén, B., 2010, "Review on Modeling Development for Multiscale Chemical Reactions Coupled Transport Phenomena in Solid Oxide Fuel Cells," *Appl. Energy*, **87**, pp. 1461–1476.
- [2] Yuan, J., Huang, Y., Sundén, B., and Wang, W. G., 2009, "Analysis of Parameter Effects on Chemical Coupled Transport Phenomena in SOFC Anodes," *Heat Mass Transfer*, **45**, pp. 471–484.
- [3] Yang, Y., Du, X., Yang, L., Huang, Y., and Xian, H., 2009, "Investigation of Methane Steam Reforming in Planar Porous Support of Solid Oxide Fuel Cell," *Appl. Therm. Eng.*, **29**, pp. 1106–1113.
- [4] Kakaç, S., Pramuanjaroenkij, A., and Zhou, X. Y., 2007, "A Review of Numerical Modeling of Solid Oxide Fuel Cells," *Int. J. Hydrogen Energy*, **32**, pp. 761–786.
- [5] Lehnert, W., Meusinger, J., and Thom, F., 2000, "Modelling of Gas Transport Phenomena in SOFC Anodes," *J. Power Sources*, **87**, pp. 57–63.
- [6] Janardhanan, V., and Deuschmann, O., 2006, "CFD Analysis of a Solid Oxide Fuel Cell With Internal Reforming," *J. Power Sources*, **162**, pp. 1192–1202.
- [7] Nagel, F. P., Schildhauer, T. J., Biollaz, S. M. A., and Stucki, S., 2008, "Charge, Mass and Heat Transfer Interactions in Solid Oxide Fuel Cells Operated With Different Fuel Gases—A Sensitivity Analysis," *J. Power Sources*, **184**, pp. 129–142.
- [8] Achenbach, E., and Riensche, E., 1994, "Methane/Steam Reforming Kinetics for Solid Oxide Fuel Cells," *J. Power Sources*, **52**, pp. 283–288.
- [9] Achenbach, E., 1994, "Three-Dimensional and Time-Dependent Simulation of a Planar Solid Oxide Fuel Cell Stack," *J. Power Sources*, **49**, pp. 333–348.
- [10] Leinfelder, R., 2004, "Reaktionskinetische Untersuchungen zur Methan-Dampf-Reformierung und Shift-Reaktion an Anoden Oxidkeramischer Brennstoffzellen," Ph.D. thesis, Universität Erlangen-Nürnberg, Erlangen-Nürnberg, Germany.
- [11] Drescher, I., 1999, "Kinetik der Methan-Dampf-Reformierung," Ph.D. thesis, Institut für Werkstoffe und Verfahren der Energietechnik, Forschungszentrum Jülich, Jülich, Germany.
- [12] Klein, J.-M., Bultel, Y., Georges, S., and Pons, M., 2007, "Modeling of a SOFC Fuelled by Methane: From Direct Reforming to Gradual Internal Reforming," *Chem. Eng. Sci.*, **62**, pp. 1636–1649.
- [13] Hussain, M. M., Li, X., and Dincer, I., 2007, "Mathematical Modeling of Transport Phenomena in Porous SOFC Anodes," *Int. J. Therm. Sci.*, **46**, pp. 48–56.
- [14] Danilov, V. A., and Tade, M. O., 2009, "A CFD-Based Model of a Planar SOFC Anode Flow Field Design," *Int. J. Hydrogen Energy*, **34**, pp. 8998–9006.
- [15] Costamagna, P., Costa, P., and Antonucci, V., 1998, "Micro-Modelling of Solid Oxide Fuel Cell Electrodes," *Electrochim. Acta*, **43**, pp. 375–394.
- [16] Hecht, E., Gupta, G., Zhu, H., Dean, A., Kee, R., Maier, L., and Deuschmann, O., 2005, "Methane Reforming Kinetics Within a Ni-YSZ SOFC Anode Support," *Appl. Catal., A*, **295**, pp. 40–51.
- [17] Aguiar, P., Adjiman, C. S., and Brandon, N. P., 2004, "Anode-Supported Intermediate Temperature Direct Internal Reforming Solid Oxide Fuel Cell I: Model-Based Steady-State Performance," *J. Power Sources*, **132**, pp. 113–126.
- [18] Haberman, B. A., and Young, J. B., 2004, "Three-Dimensional Simulation of Chemically Reacting Gas Integrated-Planar Solid Oxide Fuel Cell," *Int. J. Heat Mass Transfer*, **47**, pp. 3617–3629.